ADVANCED MATERIALS
www.advmat.de

Over-Stoichiometric Metastabilization of Cation-Disordered Rock Salts

You Wang, Alexandra Outka, Wassie Mersha Takele, Maxim Avdeev, Sami Sainio, Rui Liu, Vanessa Kee, Wonu Choe, Basirat Raji-Adefila, Dennis Nordlund, Shan Zhou, Wang Hay Kan,* Terefe G. Habteyes,* and Dongchang Chen**

Cation-disordered rock salts (DRXs) are well known for their potential to realize the goal of achieving scalable Ni- and Co-free high-energy-density Li-ion batteries. Unlike in most cathode materials, the disordered cation distribution may lead to more factors that control the electrochemistry of DRXs. An important variable that is not emphasized by research community is regarding whether a DRX exists in a more thermodynamically stable form or a more metastable form. Moreover, within the scope of metastable DRXs, over-stoichiometric DRXs, which allow relaxation of the site balance constraint of a rock salt structure, are particularly underexplored. In this work, these findings are reported in locating a generally applicable approach to "metastabilize" thermodynamically stable Mn-based DRXs to metastable ones by introducing Li over-stoichiometry. The over-stoichiometric metastabilization greatly stimulates more redox activities, enables better reversibility of Li deintercalation/intercalation, and changes the energy storage mechanism. The metastabilized DRXs can be transformed back to the thermodynamically stable form, which also reverts the electrochemical properties, further contrasting the two categories of DRXs. This work enriches the structural and compositional space of DRX families and adds new pathways for rationally tuning the properties of DRX cathodes.

1. Introduction

Among all electrochemical energy storage/conversion technologies, Li-ion batteries (LIBs) are the most well-known option for realizing the goal of electrification of transportation and a net-zero emission economy, owing to the high energy density and well-developed industrial chain of LIB productions.[1–3] The major challenge for realizing this goal is on the cathode side of state-of-the-art LIBs.[4,5] Compared to the inexpensive graphite and silicon anodes, commercialized Ni- and Co-based cathodes have been well known for their drawbacks, including limited specific capacity,[6] low earth abundance,[7] difficulties of Co-mining,[8] and toxicity of Ni- and Co-oxide compounds,[9] etc. Cation-disordered rock salt (DRXs) oxides or oxyfluorides, a series of new LIB cathode materials where Li and transition metals (TMs) are fully mixed and dispersed in a face-centered-cubic (fcc) anionic sublattice, are ideally

Y. Wang, A. Outka, W. M. Takele, B. Raji-Adefila, T. G. Habteyes, D. Chen
Department of Chemistry and Chemical Biology
University of New Mexico
Albuquerque, NM 87131, USA
E-mail: habteyes@unm.edu; chend@unm.edu

M. Avdeev
Australian Nuclear Science and Technology Organization (ANSTO)
Lucas Heights, NSW 2234, Australia

M. Avdeev
School of Chemistry
The University of Sydney
Sydney, NSW 2006, Australia

S. Sainio, D. Nordlund
SLAC National Accelerator Laboratory
Menlo Park, CA 94025, USA

R. Liu
College of Pharmacy, University of New Mexico
Albuquerque, NM 87131, USA

V. Kee, S. Zhou
Nanoscience & Biomedical Engineering
South Dakota School of Mines & Technology
Rapid City, SD 57701, USA
E-mail: shan.zhou@sdsmt.edu

W. Choe
Albuquerque Institute for Math & Science
Albuquerque, NM 87106, USA

W. H. Kan
Spallation Neutron Source Science Center
Dongguan 523803, China
E-mail: jianhx@ihep.ac.cn

W. H. Kan
Institute of High Energy Physics
Chinese Academy of Sciences
Beijing 100049, China

The ORCID identification number(s) for the author(s) of this article can be found under https://doi.org/10.1002/adma.202306396

DOI: 10.1002/adma.202306396

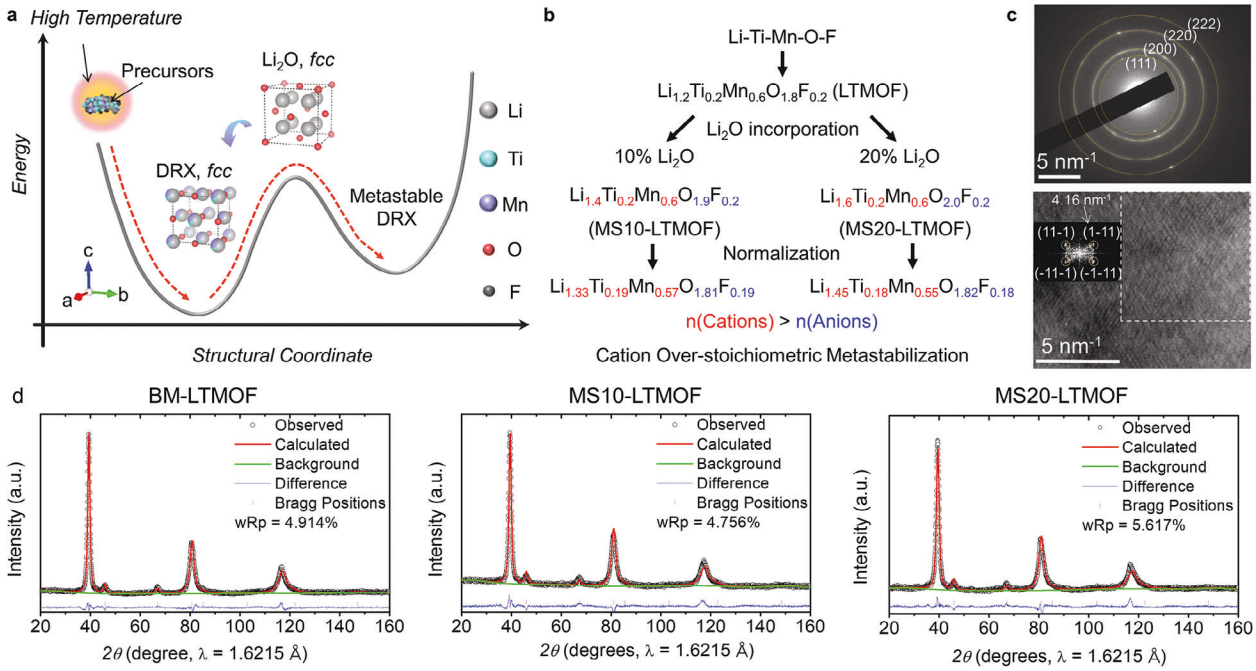

Figure 1. Schematics of metastable materials and design of the cathodes in this work. a) General energy diagram of metastable and thermodynamically stable DRXs and the metastabilization process. b) Composition design of metastable DRX cathodes based on LTMOF with different amounts of Li_2O incorporation. c) SAED pattern and TEM image with FFT pattern of MS10-LTMOF powder. d) Neutron diffraction and Rietveld simulation of pristine, MS10-, and MS20-LTMOF.

suited for resolving the challenge of LIB cathodes.[10–16] Especially, Mn-based DRXs have been under the spotlight of cathode research community in recent years, owing to their superior electrochemical performance and earth abundance of Mn.[10,17]

Compared to classic LIB cathode materials, one unique property of DRXs, especially for Mn-based, is that they can exist in either a thermodynamically stable form or a metastable form.[10,14,17,19–24] Thermodynamically stable DRXs are typically synthesized via a high-temperature solid-state synthesis approach, which "assembles" the elements from various precursors to a single phase with randomly distributed cations (**Figure 1**a). The term "metastable" means that the material is stable at room or near-room temperatures, but generally cannot be synthesized via a high-temperature solid-state synthesis process.[10,17–23,25] Metastable DRXs are typically realized via various low-temperature methods, and mechanochemistry is the most commonly applied approach.[10,12,17–23] The mechanical force decomposes the precursors, randomly disperses the elements, and generates a new metastable phase (Figure 1a). The most notable examples of metastable DRXs are a series of compositions with a general formula of Li_2TMO_2F (TM = one or mix of V, Mn, Fe, Ti, etc.).[14,20–24,26–28] Computationally, metastable DRXs generally feature a positive $\Delta E = E_{disordered} - \min(E_{ordered})$,[29] where the disordered phase is generally represented by special quasi-random structures (SQS) and $\min(E_{ordered})$ is the energy of the most stable long-range ordered phase. Experimentally, metastable DRXs typically convert to a different phase(s) at higher temperatures (i.e., an annealing process).[29–35] For example, upon heating, metastable Li_2VO_2F decomposes into $LiVO_2$ and LiF;[29] metastable $LiVO_2$ transforms to a layered phase.[34] Because of the capability of reaching a DRX phase at low temperatures, compositions of metastable DRXs are generally much more tunable than thermodynamically stable counterparts.

In the scope of metastable DRXs, because of their compositional tunability, we consider one of the most exciting opportunities is the over-stoichiometric chemical space. Herein, over-stoichiometry refers to the mole ratio between total cations to total anions being greater than 1:1, which allows the relaxation of the site balance constraint of the rock salt structure (i.e., 1:1 cation–anion ratio). While DRXs have been a research topic with fast growing interests in recent years, over-stoichiometric chemical space of DRXs is a highly underexplored field. Although a DRX cathode with a nominal composition of $Li_4Mn_2O_5$ has received a lot of attention,[36] the over-stoichiometric chemical space itself has largely not been emphasized by the community, which potentially leaves a large number of DRX compositions not explored. Because of the unexplored chemical space, the relationship between the degree of over-stoichiometry and the battery electrochemistry is mostly unknown. Fundamentally, over-stoichiometry may cause a considerable change in the scheme of charge compensation and structural evolution upon redox operation. The role of the over-stoichiometric cations in these fundamental properties is also an intriguing question. As the DRX-related research is still at a developing stage, the general category of thermodynamically stable and metastable DRX materials is largely considered as one general class of compounds by the community, leaving these important questions unanswered.

In recent years, outside of the field of battery materials research, it has been reported that over-stoichiometric cations may locate at interstitial sites in various types of fcc lattices,[37–42] hinting at the possibility of over-stoichiometric chemical spaces for rock salt structures. Moreover, a number of pioneering works have indicated that interstitial sites (e.g., tetrahedral sites) in the fcc- or near-fcc-type cathodes may be occupied by cations, which also suggests that rock salt structures may host extra cations.[43,44] All these facts infer the existence of over-stoichiometric chemical space of DRXs. In this work, we developed an approach to "metastabilize" thermodynamically stable Mn-based DRXs by introducing Li over-stoichiometry. $Li_{1.2}Ti_{0.2}Mn_{0.6}O_{1.8}F_{0.2}$ (LTMOF), a thermodynamically stable rock salt oxyfluoride with well-understood physical and electrochemical properties, was applied as the primary testbed for the approach. Our results indicate that a minor amount of over-stoichiometric Li incorporation greatly stimulates more redox activity and enables better reversibility of Li deintercalation/intercalation. The extra redox activity of the over-stoichiometric metastable DRX is backed by systematic X-ray diffraction (XRD), resonant Raman spectroscopy, and X-ray absorption spectroscopic (XAS) analyses. The same approach can be grafted to other DRX compositions and led to the similar effect of metastablization, which suggests the general applicability of the approach. Moreover, as the reverse process of metastablization, over-stoichiometric metastable DRXs can "settle down" to a thermodynamically stable form via an annealing process. This work indicates the rich diversity of chemical and structural space of Mn-based DRXs and suggests more opportunities to fine tune the thermodynamic properties to optimize their electrochemical performance.

2. Results and Discussion

2.1. Metastabilization of DRXs and Materials' Characterizations

Figure 1a shows a general schematic diagram of metastable and thermodynamically stable DRXs and the metastabilization process. Thermodynamically stable Mn-based DRX LTMOF was synthesized via a well-established high-temperature solid-state approach.[45] The cations occupy the octahedral sites (*4a*) of the fcc anionic sublattice stoichiometrically. On this basis, over-stoichiometric metastabilization of LTMOF is realized by mechanochemically milling the LTMOF with Li_2O. Similar to a rock salt structure, Li_2O is also built on an fcc anionic sublattice and also has an $Fm\bar{3}m$ space group.[46] The 2:1 cation/anion ratio of Li_2O originates from its antifluorite structure, in which the Li ions occupy all the tetrahedral sites (*8c*). Thus, Li_2O is an ideal over-stoichiometric Li source for the rock salt structure and could allow maximal accommodation of the over-stoichiometric Li in the metastable lattice. In this work, metastabilized (MS) LTMOF was realized via incorporating 10% (MS10-LTMOF) and 20% (MS20-LTMOF) mole ratios of Li_2O, as shown in Figure 1b. After normalizing the total anion stoichiometry to 2, the formulas of the MS DRXs are $Li_{1.33}Ti_{0.19}Mn_{0.57}O_{1.81}F_{0.19}$ and $Li_{1.45}Ti_{0.18}Mn_{0.55}O_{1.82}F_{0.18}$, respectively. Additionally, we synthesized LTMOF with higher mole ratios of Li_2O, including 50% and 100%, and also applied mechanochemical milling to LTMOF without extra Li_2O (denoted as BM-LTMOF). The elemental ratios of Li/Ti/Mn are quantified via inductively coupled plasma mass spectrometry (ICP-MS) analyses, shown in Table S1 (Supporting Information). The XRD patterns of the DRXs are shown in Figure S1 (Supporting Information) and demonstrate typical rock-salt-like diffraction features.

Besides XRD, a comprehensive series of physicochemical measurements were applied to investigate the structural nature of the synthesized MS DRXs. Selected-area electron diffraction (SAED) is shown in Figure 1c, consistent with the rock-salt-type diffraction pattern. The (111) family lattice fringes can be observed in the transmission electron microscopy (TEM) image, supported by the fast Fourier transform (FFT) of the lattice fringes. It is worth noting that the over-stoichiometric Li incorporation in MS10- and MS20-LTMOF is different to various reported works using Li_2O as a surface coating[47,48] and adding Li_2O in cathodes as an additive.[49–53] In both MS10- and MS20-LTMOF, no diffraction features of Li_2O are found in the MS DRXs, in contrast to the obvious Li_2O diffraction features from the coated or added Li_2O reported in various previous works. Thus, we believe that Li_2O is fused into LTMOF and Li cations are dispersed at the interstitial sites in the lattice of LTMOF. As Li is well known for its low X-ray scattering factor, we applied neutron diffraction and Rietveld refinement to LTMOF (ball-milled), MS10-, and MS20-LTMOF to evaluate the possibility of Li incorporation at interstitial sites. We found that the structural model of including extra Li at the tetrahedral sites and a minor amount of octahedral cation site vacancies (Table S2, Supporting Information) can best fit the experimental data (Figure 1d). We consider that a minor amount of octahedral cation site vacancies plays a role in stabilizing the tetrahedral Li to reduce the repulsion between the metal ions at tetrahedral sites and octahedral sites, as elaborated in Note S3 (Supporting Information). Also, we conducted neutron diffraction simulation based on the model (Figure S2, Supporting Information). Incorporation of tetrahedral Li and a minor amount of octahedral cation site vacancies leads to systematic change in intensity ratios of $I(111)/I(200)$, which is observed experimentally. Thus, based on the combination of neutron diffraction simulation and refinement, we consider the *8c* site as the most likely position for over-stoichiometric Li.

Raman spectroscopy was used to probe the effect of metastabilization from a perspective of lattice vibration. While the ideal rock salt structure is Raman inactive, any observable Raman band in DRXs is an indication of deviation from the ideal rock salt structure and can provide rich information in the structural nature of the DRXs.[23,54] In our previous work,[54] we showed that Mn-based DRXs subject to $LiCoO_2$-like layered ordering and thus demonstrate Raman bands corresponding to oxygen vibration along the lateral (i.e., "E_g") and axial (i.e., "A_{1g}") directions of layered packing (**Figure 2**b), similar to the E_g and A_{1g} of $LiNi_{0.33}Mn_{0.33}Co_{0.33}O_2$ (Figure 2a). In polarized Raman spectra, such layered ordering also leads to a decrease of relative intensity of "A_{1g}" when the polarization configuration is changed from an $Z(XX)\bar{Z}$ to $Z(XY)\bar{Z}$ configuration. These features allow us to track the change of short-range ordering in DRXs after metastabilization.

In pristine LTMOF, the "E_g" and "A_{1g}" modes locate at ≈467 and ≈607 cm^{-1}, respectively (Figure 2c). A minor band of

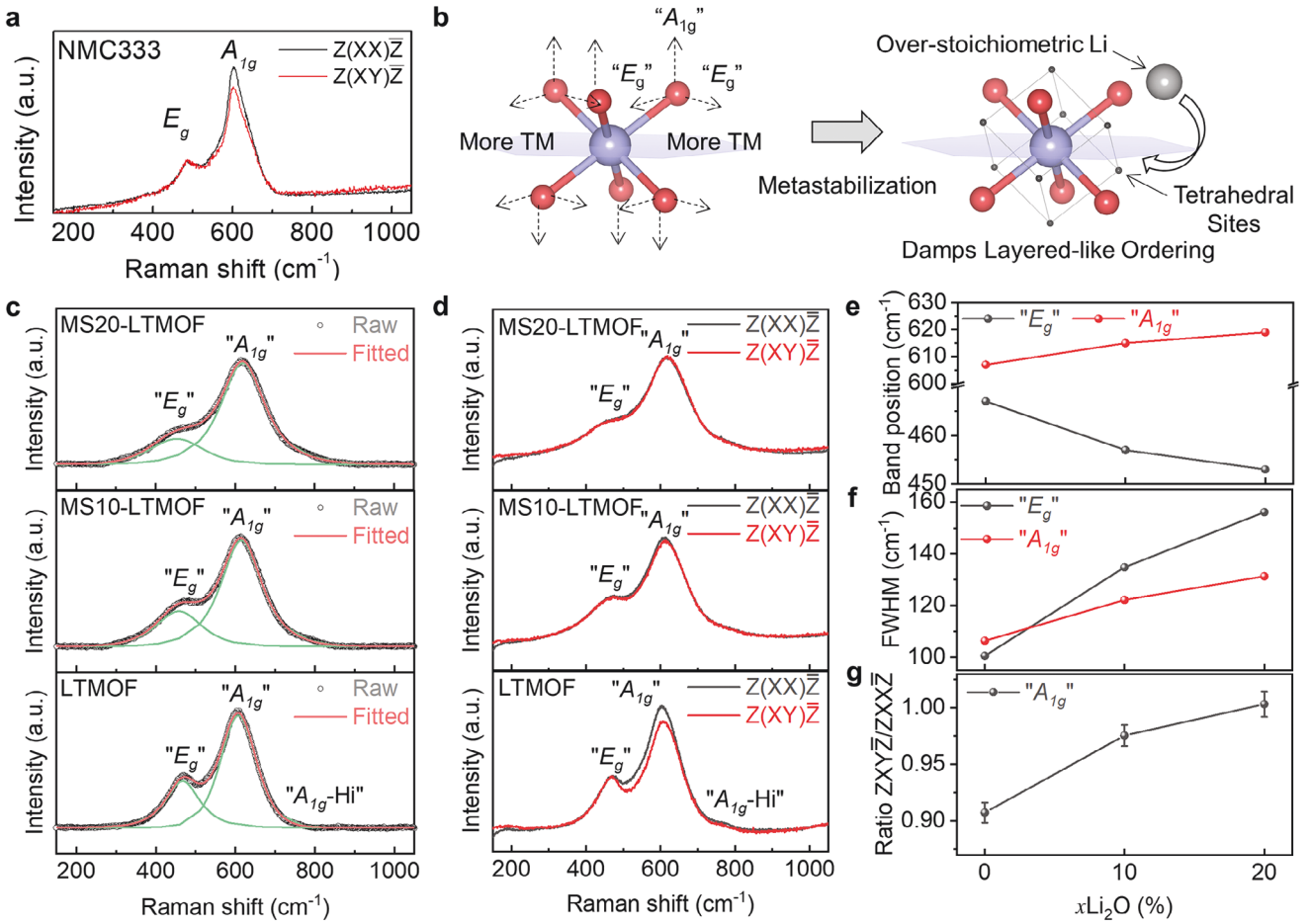

Figure 2. Structural characterizations of the pristine and metastabilized LTMOFs. a) Polarized Raman spectra of NMC333 demonstrating the A_{1g}- and E_g-like Raman bands. b) Schematic of "E_g" and "A_{1g}" vibration modes as a result of layered ordering and decrease of layered ordering due to incorporation of Li at interstitial tetrahedral sites. c) Raman spectra and spectral fitting of pristine, MS10-, and MS20-LTMOF. d) Polarized Raman spectra of pristine, MS10-, and MS20-LTMOF. The spectral intensity is normalized to the intensity of the "E_g" band. e) Band position and f) FWHM of the Raman spectra shown in (c). g) $Z(XY)\bar{Z}/Z(XX)\bar{Z}$ intensity ratio of the "A_{1g}" band of the polarized Raman spectra shown in panel (d).

LTMOF at 760 cm^{-1} corresponds to the "A_{1g}-Hi" mode, axial oxygen vibration centered at Ti.[54] In contrast to the Raman spectrum of a mixture of LTMOF and Li_2O (Note S6 and Figures S5 and S6, Supporting Information), which shows the obvious t_{2g} mode of Li_2O,[55] the MS DRXs do not present the characteristic t_{2g} band of Li_2O and demonstrate considerable spectral changes (Figure 2c), as elaborated in the following sections. First, upon over-stoichiometric Li incorporation, the "E_g" band shows a redshift, while the "A_{1g}" shows a blueshift (Figure 2e). Second, both bands show significant band broadening (increase of full width at half maximum (FWHM)) (Figure 2f,g). The "A_{1g}-Hi" mode is not observable due to the band broadening. Third, in polarized Raman spectra, the relative intensities of "A_{1g}" are less sensitive to polarization configurations after metastabilization (Figure 2d). All these phenomena can be explained by a decrease of layered anisotropy due to Li incorporation at the interstitial tetrahedral sites, as schematically shown in Figure 2b.[54] Band shifts can be explained by the extra high-wavenumber modes contributing to "A_{1g}" and extra low-wavenumber modes contributing to "E_g," as a result of occupation of tetrahedral sites by Li (Note S7 and Figure S7, Supporting Information). Band broadening is a clear indication of increased disorderness, as randomly dispersed interstitial Li will contribute to more vibration modes at these new Li sites (more discussion is in Note S7 in the Supporting Information).[56,57] The less change of relative intensity of "A_{1g}" band at different polarization conditions clearly indicates that "A_{1g}" is less polarized and layered ordering is diminished. Especially, for MS20-LTMOF, spectra are almost identical at $Z(XX)\bar{Z}$ to $Z(XY)\bar{Z}$ conditions (i.e., intensity ratio equals 1). Combining all the experimental observations mentioned above, we consider that incorporating Li_2O into LTMOF can be considered as a "structural fusion" process, a novel type of metastable ordering form.

2.2. Enhancement of Reversible Redox Activity via Metastabilization

We systematically compared the electrochemical behavior of the pristine LTMOF cathode and metastabilized ones, as shown in

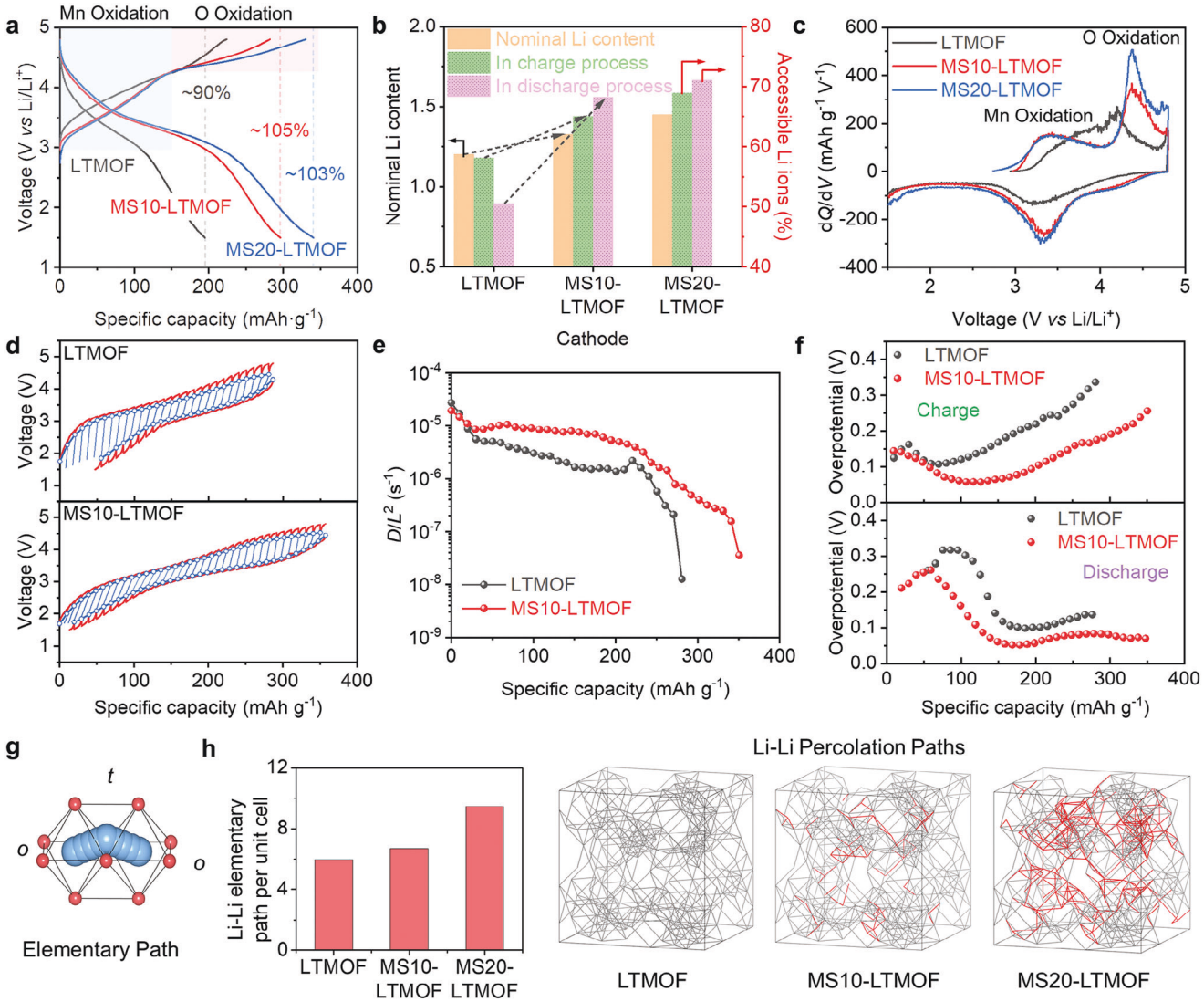

Figure 3. Electrochemistry of pristine and metastabilized LTMOF. a) Voltage profiles of pristine, MS10-, and MS20-LTMOF at the first cycle. Regions of Mn and O oxidation based on voltage profile slopes are labeled. Coulombic efficiency is labeled for each voltage profile. The current density is 20 mA g^{-1}. b) Comparison between nominal Li content and the percentage of accessible Li for the three DRXs. c) Differential capacity (dQ/dV) profiles of pristine, MS10-, and MS20-LTMOF at the first cycle. d) Voltage profiles of LTMOF (top) and MS10-LTMOF (bottom) obtained via GITT measurements. The current density is 10 mA g^{-1} and the relaxation time is 8 h. e) Calculated reciprocal of diffusion time constant ($1/\tau$) and f) overpotential based on GITT measurements. g) Schematic of elementary *o-t-o* Li transport path. h) Li transport network of pristine, MS10-, and MS20-LTMOF based on Monte Carlo simulation and the average number of Li–Li transport paths per unit cell. The over-stoichiometric Li in MS10- and MS20-LTMOFs is assumed to randomly locate at the interstitial tetrahedral sites. The red lines indicate the additional paths enabled by over-stoichiometric Li.

Figure 3. The first-cycle voltage profile of Mn-based DRXs typically has two well-separated regions with different slopes corresponding to Mn and O oxidation.[10,11] The turning point of the two different regions is ≈170 mAh g^{-1}, corresponding to completion of Mn^{3+}–Mn^{4+} oxidation (Figure 3a). The voltage profile beyond the turning point (i.e., high-voltage region) mostly corresponds to O oxidation. Both MS10- and MS20-LTMOFs demonstrate remarkable specific capacity enhancement (Figure 3a). In the first cycle, the specific discharge capacities of MS10 and MS20 LTMOFs are ≈296 and ≈341 mAh g^{-1}, respectively, in contrast to that of LTMOF (≈195 mAh g^{-1}, current density 20 mA g^{-1}). When a lower current density (10 mA g^{-1}) is used, the specific discharge capacities are enhanced to ≈326 and ≈349 mAh g^{-1}, for MS10- and MS20-LTMOF respectively, corresponding to energy densities of ≈1011 and ≈1055 Wh kg^{-1}, which are on par with the best-performing Mn-based DRXs reported so far.[17] Interestingly, their Coulombic efficiency (CE) also shows improvement. Compared to the CE of pristine LTMOF (90%), MS10- and MS20-LTMOFs both exhibit CE values close to 100% in the first cycle. This observation differs from previously reported works that employed Li_2O as a coating or additive for cathode materials,[47,49–51] which resulted in considerable overcharge due to the irreversible decomposition of Li_2O that is not integrated into the cathode lattice. Moreover, we also evaluated the degree of Li utilization

in the cathodes, calculated as the ratio of electrochemically removed/inserted Li to the nominal Li content in the composition. Compared to moderate increase of nominal Li content after metastabilization, increase of the electrochemically accessible Li, especially for the discharge process, is much more significant, as shown in Figure 3b.

Differential capacity (dQ/dV) profiles of the pristine and metastabilized LTMOF are shown in Figure 3c. After metastabilization, a significant boost is found for the discharge peak without a major change of the discharge voltage. Such an enhancement originates from the significant contribution of a high-voltage peak in the charging process. MS20-LTMOF shows more enhancement of the peak than MS10-LTMOF does. As the high-voltage oxidation peak in Li-rich cathodes has been proven to be associated with oxygen oxidation,[11,17,58] the trends of dQ/dV profiles clearly indicate that extra capacity of LTMOF after metastablization originates from oxygen redox. In parallel to the constant current charge–discharge measurements, we applied galvanostatic intermittent titration technique (GITT) to evaluate the role of metastabilization on the kinetic behavior. GITT profiles for pristine and MS-10 LTMOF in the first cycle are shown in Figure 3d. The magnitude of voltage drop before and after relaxation (after excluding IR drop) can be used to evaluate the kinetics of diffusion.[59,60] Figure 3e shows the reciprocal of diffusion time constant ($1/\tau = D/L^2$, τ: diffusion time constant, L: diffusion length) of the charging process indicating that MS10-LTMOF has considerably greater diffusion coefficients than LTMOF. Meanwhile, the extent of hysteresis, indicated by the difference of equilibrium voltage between charge and discharge (the enclosed area in Figure 3d), is considerably alleviated for MS10-LTMOF than the pristine one. Additionally, the voltage drop of each relaxation step (including the IR drop) of MS10-LTMOF is also considerably lower than that of the pristine one, for both charge and discharge processes (Figure 3f).

We believe the considerably boosted electrochemical performance of MS LTMOFs originates from the change of intrinsic properties of the rock salt lattice. First, we analyzed the possibility of extrinsic materials properties contributing to the difference in electrochemical behavior, including specific surface area, porosity, and particle size. N_2 adsorption experiments indicate that the surface area and porosity of the pristine, MS10-, and MS20-LTMOF electrode composites are largely comparable (Note S10 and Figure S14, Supporting Information). Scanning electron microscopy (SEM) images also indicate that the three electrode materials do not differ greatly in particle size (Figure S13, Supporting Information). Moreover, we measured the electrochemical behavior of mechanochemically ball-milled LTMOF without Li_2O and found no drastic improvement of specific capacity (Note S8 and Figures S8, S10, and S11, Supporting Information). Thus, we consider the key to the higher specific capacity of MS DRXs is the change of Li-ion transport schemes. Based on an octahedral–tetrahedral–octahedral (*o-t-o*) elementary transport path (Figure 3g), Li conduction in DRXs is strongly sensitive to the nominal Li content, as a higher Li content generally enhances the likelihood of a Li site accessible to other Li sites.[13,61] Metastabilizing the LTMOF by slightly increasing the Li content in the interstitial tetrahedral sites allows more Li percolation within the disordered lattice. To demonstrate the point, we performed simple Monte Carlo simulation experiments (Note S11 and Figure S15, Supporting Information). The interstitial Li adds transport paths in addition to the *o-t-o* percolation network and thus increases the possible nearest-neighbor Li exchange pairs per unit cell, as shown in Figure 3h.

To further evaluate the role of over-stoichiometry in Li transport, we conducted rate capability measurement of the cathodes mentioned above. The voltage profiles of pristine and MS20-LTMOF, highlighting the effect of over-stoichiometry on rate capability, are shown in **Figure 4**. The complete set of voltage profiles are shown in Figure S8 (Supporting Information). While a drop of specific capacity at higher current rates is commonly observed, the performance retention at higher current rates is greatly improved for MS LTMOF. In contrast, the specific capacity of pristine and BM-LTMOF suffer from a drastic drop, leading to a much greater performance difference among these cathodes. Moreover, the dQ/dV peak profiles of MS LTMOF, especially for MS20-LTMOF (Figure 4b), are much better maintained at higher current rates, whereas the redox peaks of pristine and BM-LTMOF suffer from considerable polarization and decrease of differential capacity. These experimental observations suggest that the redox processes of Mn and O redox of MS LTMOF are not greatly affected by a higher current rate. Figure 4c summarizes the first-cycle specific discharge capacity of the cathodes as a function of current rate. Specifically, at a high current rate of 500 mA g^{-1}, the specific discharge capacity of pristine, ball-milled, MS10-, and MS20-LTMOF are 79, 125, 195, and 248 mAh g^{-1}. The evolution of discharge voltage is also shown in Figure 4d. While the variation of discharge voltage among the cathodes at a lower current rate is minimal, the contrast of discharge voltage is very significant at high current rates of 500 and 1000 mA g^{-1}. The variation of the discharge voltage agrees well with the evolution of dQ/dV profiles as a function of current rate.

Additionally, we make a note that the cycling stability of LTMOFs is compromised after metastabilization at low current rate, as elaborated in Note S8 (Supporting Information). The most likely reason is the high contribution of oxygen redox MS LTMOF causes significant electrolyte degradation, which has been a well-known detrimental factor for long-term cycling of DRXs.[11,17,62] Nonetheless, the performance of MS LTMOFs, including both specific discharge capacity and discharge voltage, can be well-retained as a function of cycling at higher current rates (Figures S10 and S11, Supporting Information), which maintains the large performance contrast between pristine/BM and MS10-/MS20-LTMOFs with extended cycles.

Besides the MS10- and MS20-LTMOF discussed in the abovementioned texts, we also explored the possibility of incorporating more Li_2O into the LTMOF lattice (Note S9 and Figure S12, Supporting Information). We found that incorporating Li_2O with a higher mole ratio more than 20% can lead to significant overcharge, thus greatly lowering the Coulombic efficiency, and even leads to a decrease of specific discharge capacity (Figure S12, Supporting Information). These results clearly indicate that the extra Li cannot be reversibly utilized in these cases, most likely, because the extra Li is not "fused" into the rock salt lattice, which is similar to previous studies that use Li_2O as a coating or an additive.[47,49,50]

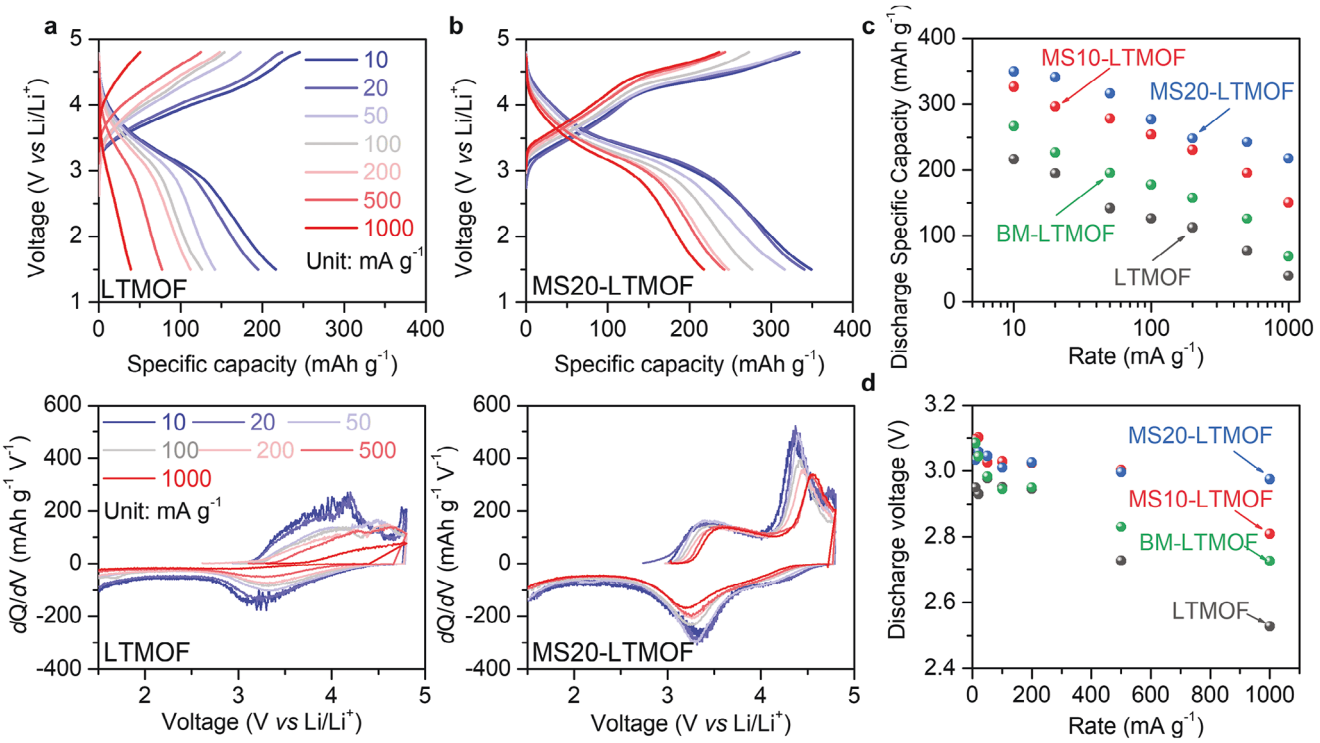

Figure 4. Rate capability of LTMOF after over-stoichiometric metastabilization. a) First-cycle voltage profiles (upper) and dQ/dV profiles (lower) of pristine LTMOF at the various current densities. b) First-cycle voltage profiles (upper) and dQ/dV profiles (lower) of MS20-LTMOF at the various current densities. c) Specific discharge capacities of pristine, ball-milled, MS10-, and MS20-LTMOF as a function of current densities. The current density is shown in a logarithm scale to highlight the evolution. d) Discharge voltage of pristine, ball-milled, MS10-, and MS20-LTMOF as a function of current density. The current density is shown in a linear scale to highlight the contrast of discharge voltage at high current rates.

2.3. Energy Storage Mechanism of Metastabilized DRX

We conducted a series of physicochemical analyses to unravel the structural features associated with the extra capacity caused by over-stoichiometric metastabilization from different perspectives. **Figure 5**b shows the evolution of ex situ XRD at various states of charge and discharge for MS10-LTMOF. The evolution for pristine LTMOF is shown in Figure S16 (Supporting Information). During the charge and discharge processes, the XRD peaks consistently shift to higher and lower angles, corresponding to lattice shrinkage and expansion due to Li deintercalation and intercalation, respectively. The evolution of lattice parameters is summarized in Figure 5c. The extent of lattice shrinkage after the cell is fully charged (4.8 V) is 2.3% for pristine LTMOF and 2.9% for MS10-LTMOF. Moreover, MS10-LTMOF shows a higher lattice dimension at the fully discharged state (1.5 V) than that of the open-circuit voltage (OCV) state, while the pristine LTMOF shows a lower lattice dimension compared to the OCV state. The more significant change in the lattice dimension for MS10-LTMOF is a result of a greater amount of reversible Li intercalation/deintercalation. Also, the larger postdischarge lattice size than the OCV state for MS10-LTMOF is consistent with its Coulombic efficiency greater than 100%.

We also investigated the structural change from a perspective of lattice vibration via Raman spectroscopy (MS10-LTMOF in Figure 5d, and pristine LTMOF in Figure S16 in the Supporting Information). The general trend of Raman spectral evolution is that charge (delithiation) and discharge (lithiation) lead to blueshift and redshift, respectively, for both "A_{1g}" and "E_g" bands. This trend is a result of the mode-hardening effect caused by lattice shrinkage, which is experimentally shown as bands shift toward higher wavenumber regions, and vice versa. The extent of the band shift of MS10-LTMOF between the fully charged/discharged states is slightly more significant than that of the pristine LTMOF (Figure 5e), consistent with the XRD analyses. While the spectral profiles of pristine LTMOF are largely unchanged at various charged/discharged states (Figure S16, Supporting Information), the spectrum of MS10-LTMOF at 4.8 V is distinctive to those at other states. The "A_{1g}" band is much narrower and harder. The "E_g" disappeared and is replaced by a very broad band at lower wavenumbers. Among common Mn oxide compounds, the closest match we found for the narrow feature and the band position of the "A_{1g}" at 4.8 V is the A_{1g} mode of spinel Mn_3O_4 (Figure 5g), which corresponds to oxygen vibration stretching close to/away from the octahedral Mn site.[63,64] The spectral contrast at 4.8 V suggests different ordering schemes of pristine and MS10-LTMOF at the fully charged states (i.e., different types of deviation from the ideal Raman-inactive O_h octahedral symmetry). Fully charged LTMOF still presents the layered-like Raman features indicating that the unique direction of the TMO_6 octahedra ordering is along the threefold axis of the octahedra (D_{3d}-like), similar to $LiCoO_2$.[65] The narrower and harder "A_{1g}" bands of fully charged MS10-LTMOF indicate that the unique direction of TMO_6 octahedra is along the fourfold axis

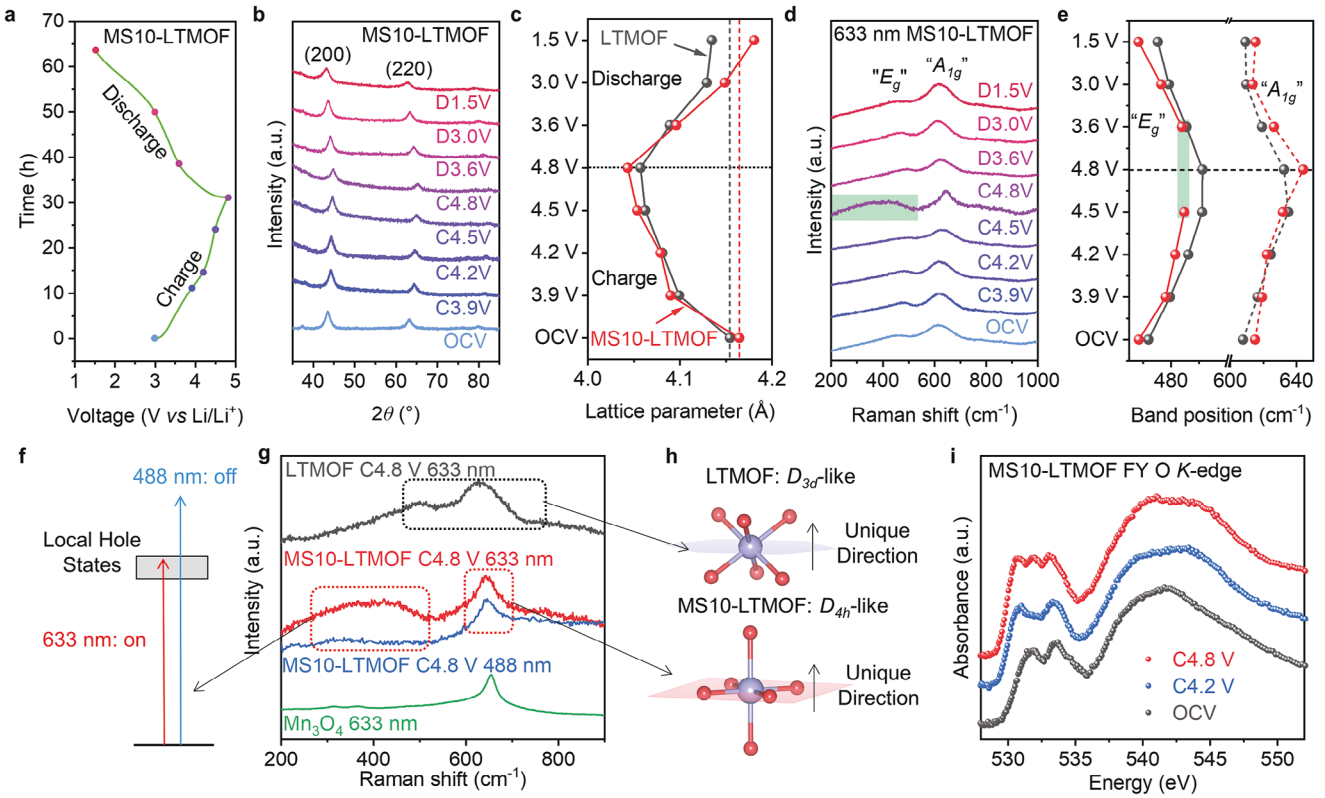

Figure 5. Electrochemically induced structural changes of MS10-LTMOF. a) Charge–discharge voltage profile of MS10-LTMOF and selected states of charge/discharge for ex situ characterizations. b) Ex situ XRDs of MS10-LTMOF electrodes at various charged (C) and discharged (D) states. Note that the OCV state refers to the as-prepared electrode. c) Evolution of lattice parameters of LTMOF and MS10-LTMOF. d) Ex situ Raman spectra of MS10-LTMOF electrodes at various charged and discharged states. e) Evolution of Raman band positions of LTMOF and MS10-LTMOF. f) Schematic of resonant Raman effect of MS10-LTMOF at the fully charged state with different laser excitation energies. g) Raman spectra of pristine and MS10-LTMOF at the fully charged state compared to that of Mn_3O_4 spinel. h) Schematic of ordering schemes for pristine and MS10-LTMOF at the fully charged state. i) O *K* edge XAS of MS10-LTMOF at various charged states measured using the fluorescent yield (FY) mode.

of the octahedra (i.e., D_{4h}-like), suggesting elongation and compression the Mn—O lengths along *z*- and (*x*, *y*)-directions, respectively. As Mn is randomly dispersed crystallographically, such distortion does not appear as notable changes in XRD.

It should be noted that, at a high voltage cutoff of 4.8 V, the involvement of oxygen oxidation could cause reduction of transition metal to a lower oxidation state. To evaluate the possible contribution of lower-valence Mn in the Raman spectrum at 4.8 V, we conducted linear combination fitting of the Mn *L* edge XAS spectra, as shown in Figure S17 (Supporting Information). It is well known that Mn *L* edge XAS (collected at total electron yield, TEY mode) probes the surface region of samples and thus is ideally suited to probe the oxygen-oxidation-induced TM reduction. The linear combination fitting indicates that the contributions of Mn(IV), Mn(III), and Mn(II) are 69%, 23%, and 8% for 4.2 V, and 71%, 21%, and 8% for 4.8 V, respectively. The largely similar spectral features at 4.2 and 4.8 V agree with the fact that the voltage profile turning point (i.e., from Mn oxidation to O oxidation) is near ≈4.2 V. It also suggests that the sharp Raman spectral feature at 4.8 V originates from the intrinsic bonding structure at that state. Such a change of bonding geometry is likely to be related to the change of the electronic structure of the coordinating oxygen, given the considerable contribution of oxygen oxidation at 4.8 V. Unlike the sharp "A_{1g}" at the fully charged state, the broad low-wavenumber band is excitation energy sensitive (i.e., resonance effect), as shown in Figure 5f. The resonance effect suggests the existence of local electronic states. Considering the contribution of oxygen oxidation at the fully charged state, we consider that the broadband arises from localized vibration mode on localized oxygen holes (i.e., Mn—O^-),[66,67] which are resonantly enhanced at a lower excitation energy (≈633 nm, 1.96 eV). With a higher Raman excitation energy (i.e., 488 nm, ≈2.54 eV), the broad low-wavenumber band is not observable, which could be a result of the off-resonance excitation. After the cell is fully discharged at 1.5 V, the spectral features and band positions largely recover to those at the OCV states for both pristine and MS10-LTMOF, indicating the reversibility of Li intercalation and deintercalation.

The contribution of oxygen oxidation in MS10-LTMOF is further supported by oxygen *K* edge XAS measurements. At the OCV state, the two obvious low-energy absorption peaks correspond to the O_{1s} electron transition to Mn—O hybrid orbitals in an octahedral field with t_{2g} and e_g symmetries,[68,69] respectively. At 4.2 V, the two peaks shift to lower energies, indicating removal of electrons in the Mn—O hybrid orbitals and consistent with the spectral features of high-spin Mn^{4+}.[68,69] It should be noted that the

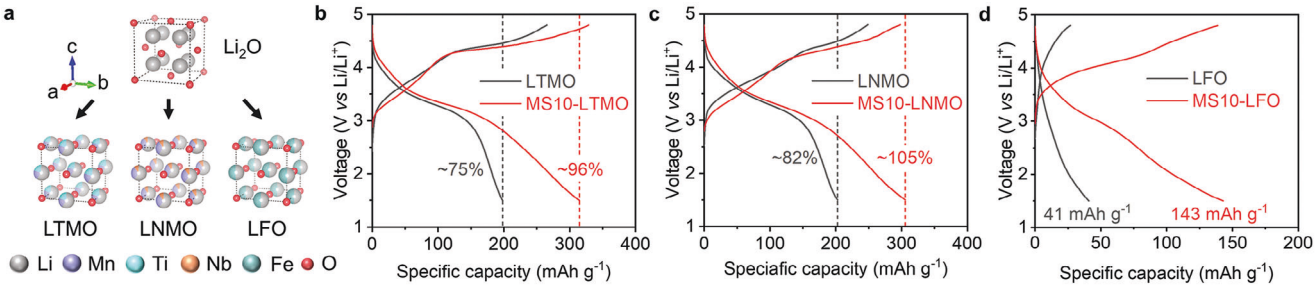

Figure 6. Extending over-stoichiometric metastabilization to other DRX compositions. a) Schematic of extending the metastabilization to LTMO, LNMO, and LFO via incorporating over-stoichiometric Li. b–d) Voltage profiles of LTMO (b), LNMO (c), and LFO (d) before and after over-stoichiometric Li incorporation.

attribution of the two peaks to the respective transitions is merely a general assignment, and the two peaks are a result of an overlap of multiple spin states.[68,69] At 4.8 V, a new absorption peak at ≈531 eV appeared. Extensive resonant inelastic X-ray scattering studies have indicated that a unique X-ray absorption/emission feature at 531/524 eV is the signature of oxidized oxygen and corresponds to the transition to a specific excitonic state (σ^* electron and π hole) as a result of O—O dimer.[70] While we cannot determine the emission energy of each absorption peak, we consider that the extra absorption peak at 531 eV corresponds to the feature of oxidized oxygen. This assignment is further supported by the fact that the change of Mn *L* edge XAS is minimum between 4.2 and 4.8 V (Note S17 and Figure S17, Supporting Information), and Ti has been well known as a redox inactive element in DRX cathodes.[71,72] Thus, the XAS results support the Raman spectroscopic findings and corroborate the mechanistic analyses of MS LTMOF.

Additionally, we performed more spectral analyses of the first discharged state to probe the structural details related to higher CE of MS LTMOF. We believe the most likely reason is that MS LTMOF allows more Li stored at the tetrahedral sites at the fully discharged state. In a recent separate study,[73] we found that t_{2g} modes of $LiMn_2O_4$ spinel can be selectively enhanced by near-IR laser (785 nm) excitation, including the t_{2g} mode of tetrahedral Li, as shown in Note S14 and Figure S18 (Supporting Information). The fully reduced (1.5 V) MS10-LTMOF demonstrates high-intensity low-wavenumber bands with similar characteristics of the two t_{2g} modes of $LiMn_2O_4$. Such a phenomenon further suggests that the higher CE and discharge capacity of MS10-LTMOF originate from extra electrochemically intercalated Li locating at the tetrahedral sites.

2.4. Extending the Metastabilization

To examine the general applicability of the metastabilization route, we have also extended the method to other DRXs. Specifically, we chose three compositions, $Li_{1.2}Ti_{0.4}Mn_{0.4}O_2$ (LTMO), $Li_{1.2}Nb_{0.2}Mn_{0.6}O_2$ (LNMO), and $LiFeO_2$ (LFO) (**Figure 6**a). A common feature among these DRX is that their electrochemical performance is mostly throttled by the limited Li content in their structures. For the Mn-based DRXs, the 1.2 Li per formula are near the boundary between a percolating and a nonpercolating Li network.[13] The Li content in $LiFeO_2$ (1.0 Li per formula) is in the nonpercolating range. After over-stoichiometric metastablization, XRD and Raman features of these DRXs demonstrate similar changes compared to the changes of LTMOF (Note S15 and Figures S19–S22, Supporting Information). A moderate increase of Li content via incorporating 10% mole ratio of Li_2O significantly boosts the first-cycle specific discharge capacity, from 198, 203, and 41 to 314, 306, and 143 mAh g^{-1}, for LTMO, LNMO, and LFO, respectively. These changes correspond to 59% (LTMO), 51% (LNMO), and 249% (LFO) enhancements of specific discharge capacity (Figure 6b–d). Moreover, metastablization also improves the Coulombic efficiency for Mn-based DRXs, from ≈75% to ≈96% and from ≈82% to ≈105% for LTMO and LNMO, respectively. The Coulombic efficiency for MS10-LFO is also near 100%. More electrochemical data are shown in Figure S23 (Supporting Information). These electrochemical results indicate the general applicability of incorporating over-stoichiometric Li in DRX lattice to increase the reversible capacity, in contrast to the overcharging phenomenon as a result of adding Li_2O as an additive in cathodes.

2.5. Applying "Restabilization"

To investigate the reverse process of metastabilization, we also studied the route of "restabilization" of metastabilized DRXs, as schematically shown in **Figure 7**a (more details are elaborated in Note S16 and Figures S24 and S25 in the Supporting Information). First, we prepared a DRX with the same targeting composition of MS10-LTMOF via the traditional solid-state synthesis route (SS10-LTMOF), aiming to examine the possibility of obtaining a similar electrochemical behavior of MS10-LTMOF. The voltage profile and d*Q*/d*V* profile of SS10-LTMOF are drastically different to those of MS10-LTMOF (Figure 7b,c). The first-cycle specific discharge capacity is ≈164 mAh g^{-1} with a Coulombic efficiency of ≈68%. The stark contrast may arise from the possible fact that MS10-LTMOF is not obtainable using a solid-state synthesis route. Moreover, we also annealed the MS10-LTMOF, aiming to "restabilize" the metastable DRX and evaluating the change of electrochemical behavior. Notably, annealing the over-stoichiometric metastable rock salts still leads to an apparent rock-salt-like phase, instead of converting to a phase with long-range ordering or being decomposed to other phases. This observation is different to many other metastable DRXs that change to a nondisordered phase(s) after annealing.[29,34,35] It also suggests

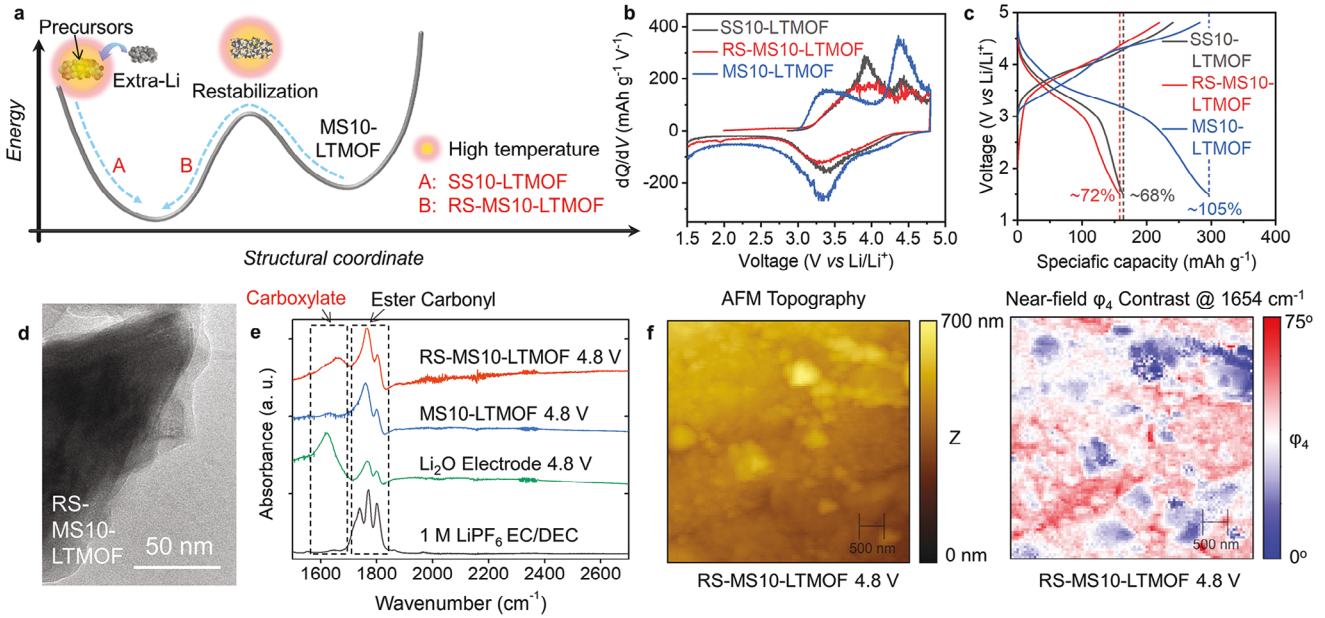

Figure 7. Applying restabilization to MS LTMOF. a) Schematic of the attempt to synthesize the composition of MS10-LTMOF via a solid-state approach by adding extra Li source (i.e., SS10-LTMOF) and the route of restabilizing MS10-LTMOF via an annealing process (i.e., RS-MS10-LTMOF). b) Differential capacity and c) voltage profiles of SS10-LTMOF and RS-MS10-LTMOF compared to those of MS10-LTMOF. d) TEM image of RS-MS10-LTMOF showing the particle is covered with a low-contrast coating. e) ATR-FTIR spectra of various cathodes (including a bare Li_2O electrode) at the fully charged state compared to the spectrum of the electrolyte. Two important wavenumber regions, including carboxylate and ester carbonyl, are highlighted. Voltage profile of the Li_2O electrode is also shown. f) AFM topography and contrast of phase angle of s-SNOM signal (demodulated at fourth harmonics) excited by a 1654 cm^{-1} IR laser for a 5 × 5 μm^2 area of an RS-MS10-LTMOF electrode at the fully charged state.

that, for DRXs, the metastable–thermodynamically stable phase conversion is not limited to DRX-ordered phase and can be extended to DRX (metastable)–DRX (thermodynamically stable). For RS-MS10-LTMOF, both specific discharge capacity (≈158 mAh g^{-1}) and CE (≈72%) demonstrate a drastic decrease compared to those of MS10-LTMOF (Figure 7c), indicating that a significant amount of reversible capacity is lost. ICP-MS measurements indicate that relative Li contents of both RS-MS10-LTMOF and SS10-LTMOF are significantly greater than that of LTMOF (Table S1, Supporting Information). Moreover, we measured the TEM images of RS-MS10-LTMOF (Figure 7d) and SS10-LTMOF (Figure S26, Supporting Information) and found that the particle surface is often coated with a low-contrast layer, which is most likely Li- and O-containing species that are not fully incorporated into the bulk rock salt structure. The decomposition of such surface species is the most likely reason for the lower CE.

To understand this effect, we performed infrared (IR) absorption to probe the chemical information of cathode–electrolyte interface (CEI), which is known to be directly related to the Coulombic efficiency of cathode materials, shown in Figure 7e. In the wide-field IR absorption spectra, both MS10-LTMOF and RS-MS10-LTMOF demonstrate peaks between 1700 and 1800 cm^{-1}, indicating ester species of the CEI. The spectrum of RS-MS10-LTMOF demonstrates a significantly different feature, compared to the spectra of MS10-LTMOF and the electrolyte, at 1654 cm^{-1}. Such a feature is a clear indication of formation of carboxylate species as a result of carbonate ester decomposition. We believe that the electrochemistry-induced decomposition of trace surface Li- and O-containing species causes the electrophilic attack from the surface oxygen toward the electron-rich aliphatic ester, leading to carboxylates. To evaluate the possibility, we tested the electrochemical behavior of Li_2O electrodes and observed the considerably irreversible charge behavior (Figure S27, Supporting Information). IR absorption features in the carboxylate region were also observed for the charged Li_2O electrodes.

Moreover, we conducted scattering-type scanning near-field optical-microscopy-based IR (s-SNOM-IR) mapping to probe the distribution of CEI chemical species for RS-MS10-LTMOF at the fully charged state (Figure 7f). The emergence of near-field IR absorption technique allows a spatial resolution up to 10 nm, which greatly exceeds the diffraction limit of optical imaging while providing vibrational mapping using soft IR light.[74–76] Such a unique power offers the opportunity to elucidate the nanoscale heterogeneity of interfacial species distribution. Fundamentals related to s-SNOM imaging are described in Note S18 and Figure S29 (Supporting Information). The atomic force microscopy (AFM) images acquired synchronously with s-SNOM-IR measurement depict the height profile of the electrode in a 5 μm × 5 μm area. Nanoscale distributions of carboxylate at 1654 cm^{-1}, acquired via mapping the phase angle of scattered s-SNOM signal (demodulated at fourth harmonics), reveal the nanoscale domains where strong infrared light absorption of carboxylate function groups occurs. The observed heterogeneity of carboxylate deposition suggests that electrode particle orientation, morphological factors, and topography may interplay and cause the nonuniform decomposition of electrolyte solvent. The s-SNOM IR imaging expands the wide-field spectroscopic signatures to nanoscale images of functional groups and reveals the reason for

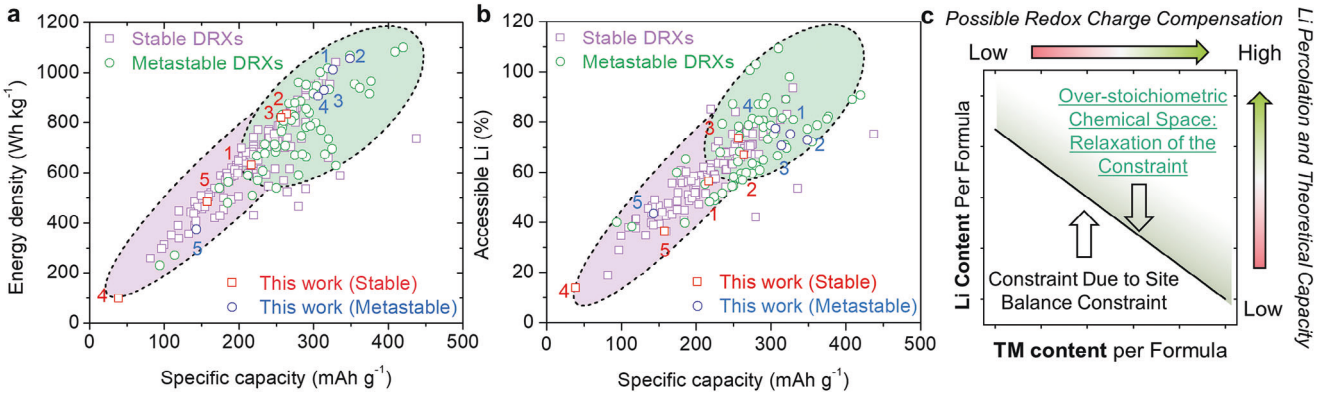

Figure 8. Review of electrochemical properties of thermodynamically stable and metastable DRXs. a) Energy density vs specific capacity of reported thermodynamically stable/metastable DRX cathodes and the DRXs in this work. b) The percentage of utilizable Li vs specific capacity of reported thermodynamically stable/metastable DRX cathodes and the DRXs in this work. Labeled numbers: blue: 1: MS10-LTMOF, 2: MS20-LTMOF, 3: MS10-LTMO, 4: MS10-LNMO, 5: MS10-LFO. Red: 1: LTMOF, 2: LTMO, 3: LTNO, 4: LFO, 5: RS-MS10-LTMOF. c) Schematics of relaxation of site-balance constraint of rock salt structures enabled by over-stoichiometric chemical space and its potential in enabling both high redox activity, Li percolation, and theoretical capacity.

the lower CE of RS-MS10-LTMOF from a spectral imaging perspective.

2.6. A General Comparison of Thermodynamically Stable and Metastable DRXs

Our experimental data suggest that properties of thermodynamically stable and metastable DRX materials, as indicated by specific discharge capacity, ratio of utilizable Li, and the energy storage mechanism, can be distinctly different. Such a difference also implies that there are significant differences between the currently reported thermodynamically stable DRX materials and metastable counterparts, which have not been emphasized so far. To comprehensively discuss the two categories of cathodes, we conducted a performance data consolidation based on literature values and incorporated our findings into the analyses, as shown in **Figure 8**. Specifically, the first-cycle discharge energy density and the ratio of utilizable Li of various DRXs as a function of first-cycle specific discharge capacity are shown in Figure 8a and Figure 8b, respectively. The summarized DRXs span various redox-active elemental compositions, including Mn^{4+}, Mn^{3+}, Mn^{2+}, Ni^{2+}, Mo^{3+}, V^{3+}, Cr^{3+}, and Fe^{3+}. The details of the data are elaborated in Note S20 and Tables S3 and S4 (Supporting Information).

Here, we refer thermodynamically stable and metastable DRXs in Figure 8 to the DRXs synthesized via high-temperature solid-state routes and low-temperature mechanochemical routes, respectively, to distinguish their differences in terms of the ability to exist at high temperatures. Also, we make a note that the detailed electrochemical testing and electrode fabrication parameters, such as voltage window, current rate, and carbon mixing, of these works are not consistent. Thus, it is not reasonable to compare point to point of the data in Figure 8. Although the data points in Figure 6 are highly scattered due to the variation of the reported DRXs, the significance of the difference between thermodynamically stable and metastable compounds is noteworthy. First, as shown in Figure 8a, the specific discharge capacity and energy density of metastable DRXs are generally higher than those of the thermodynamically stable counterparts, indicating that the metastability enhances the discharge capacity without compromising the discharge voltage. The fact that most of the top-performing DRXs were made via the mechanochemical route aligns with the trend.[12,17,77,78] Second, the higher specific discharge capacity of metastable DRXs is positively correlated to the increase of the ratio of utilizable Li, suggesting that metastability unlocks more redox activity by rendering a greater portion of Li in DRXs electrochemically utilizable. It is possible that metastability achieved through mechanochemistry may lead to distinctly different short-range ordering patterns compared to solid-state synthesis, even for very similar compositions or stoichiometries.[54,79–81] This could be the fundamental reason for the more utilizable Li of metastable DRXs. The contrast of the DRXs used in this work (highlighted in Figure 8) is consistent with both trends shown in Figure 8. Note that the data consolidation shown in Figure 8 does not include cycling stability, which is a critical electrochemical parameter of DRXs. Based on the comparative analyses, it can be inferred that metastable and thermodynamically stable DRXs can be classified into two classes of materials, despite their similar long-range cation disorderness in fcc lattices. Thus, rock salt structures are a unique class of materials that can exist either in a stable and an over-stoichiometric metastable form, and the two forms can interconvert with each other. Such a property is different to other metastable cathode materials reported in recent years (e.g., antifluorite-like cathodes)[82,83] and has been rarely found in other metastable structures.

Given the contrast of thermodynamically stable and metastable DRXs mentioned above, over-stoichiometric metastable DRXs may open up extra opportunities in designing new DRXs. The major advantage of over-stoichiometric DRX is shown in Figure 8c. In the scope of traditional rock salts ($Li_{1+x}TM_{1-x}O_2$), there is always a trade-off between TM content and Li content because of the site balance constraint (i.e., n(Li) + n(TM) = 2). The site balance constraint poses a negative linear correlation (Figure 8c) between Li content, the

key factor that determines the maximum possible capacity, and the redox-active TM content, the key factor that determines the maximum possible TM redox contribution. With the site balance constraint, increasing redox active TM to introduce more redox activity will cause a low Li content, which will cause undesired Li transport. The typical example is the poor electrochemical performance of stoichiometric rock-salt-type $LiFeO_2$ (Figure 6d). On the other hand, increasing the Li content to enhance the Li transport inevitably causes highly limited TM redox contribution, which can lead to very poor electrochemical behavior as well. To demonstrate this point, we synthesized a Ti–Mn-based DRX $Li_{1.34}Ti_{0.58}Mn_{0.08}O_{1.9}F_{0.1}$. Its Li content is the highest Li content that we can achieve for stoichiometric Ti–Mn-based DRXs and very close to the charge balance limit, which inevitably leads to a very low Mn content. Its first-cycle voltage profile is compared to that of MS10-LTMOF (Li content 1.33 per formula) in Figure S30 (Supporting Information). Because of the low Mn content in $Li_{1.34}Ti_{0.58}Mn_{0.08}O_{1.9}F_{0.1}$, the amount of charge compensation for Li deintercalation is very limited, leading to highly limited specific capacity, although the amount of Li is abundant. In contrast, MS10-LTMOF is not subjected to such a limitation, by featuring high redox activity and high Li content at the same time. Thus, the generally applicable over-stoichiometric metastablization route allows the relaxation of the site balance constraint and enhances the Li transport and Li utilization for DRX compositions without lowering the TM redox contribution (Figure 8c), by expanding the percolation theory to the over-stoichiometry chemical space. It will offer the possibility of unlocking more redox activity without a capacity/redox contribution trade-off and allows DRXs to expand to more diverse compositions, potentially stimulating the discovery of more high-performance DRX cathodes.

3. Conclusion

We have located a new route to "metastabilize" DRXs by introducing Li over-stoichiometry and expanded the diversity of DRX cathode materials. Based on a well-known DRX (LTMOF) as the testbed, we found that introducing a moderately small amount of extra Li (10–20% mole ratio) via mechanochemistry allows the relaxation of the site-balance constraint of solid-state-synthesized DRXs. The over-stoichiometric metastabilization increases the degree of disordering, enhances the amount of electrochemically utilizable Li, and unlocks more redox activity of DRXs. Relying on a systematic combination of diffraction and spectroscopic analyses, we found that Li deintercalation in metastabilized LTMOF involves more significant lattice dimension change, more redox activity from oxygen, and changes of the short-range ordering scheme at the fully charged state. After extending the metastabilization approach to other DRX compositions, we found that the developed method is a generally applicable option for DRXs to overcome the lack of Li percolation and to boost the amount of electrochemically utilizable Li. By consolidating our results and the extensive electrochemical data of various reported works focusing on DRX cathodes, we found that the performance of metastable DRXs is systematically higher than that of thermodynamically stable ones, suggesting the fundamental difference between the two categories of DRXs. An important avenue for future research would be to conduct more exploration of over-stoichiometric chemical space of DRXs and explore the relationship between composition, structure, functionality, and mechanism in the over-stoichiometric chemical space. Fine-tuning the structure and properties of over-stoichiometric DRXs via various materials/particle engineering techniques[84,85] is also highly worth exploring. Findings of this work suggest a new controllable variable to tune the properties of DRXs and provide further promise for utilizing DRXs as a means to address outstanding challenges in LIB cathodes.

4. Experimental Section

Full experimental procedures can be found in the Supporting Information.

Supporting Information

Supporting Information is available from the Wiley Online Library or from the author.

Acknowledgements

This work was financially supported by University of New Mexico new faculty startup award, research allocation committee award, and Oak Ridge Associated Universities Ralph E. Powe Junior Faculty Enhancement Award. Use of the Stanford Synchrotron Radiation Lightsource, SLAC National Accelerator Laboratory is supported by the Office of Science, Office of Basic Energy Sciences of the U.S. Department of Energy under Contract No. DE-AC02-76SF00515. Acquisition of the quantum cascade laser used for s-SNOM IR imaging in this work was supported by NSF award 2154617. S.Z. was supported by faculty startup award at South Dakota School of Mines and Technology. The ICP-MS instrument was supported in part by NIH P20GM130422 and P30ES032755. The authors greatly appreciate the neutron beamtime granted from ECHIDNA in ANSTO.

Conflict of Interest

The authors declare no conflict of interest.

Author Contributions

D.C., T.G.H., W.H.K., and S.Z. conceived the project and designed the experiments. Y.W. and A.O. carried out the main experiments and collected the data. S.S. and D.N. collected the XAS data. W.C. and B.-R.A. helped with the synthesis of the cathode material, cell assembly, and XRD data collection and analyses. M.A. conducted neutron diffraction experiments and W.H.K. performed data analyses of neutron diffraction and bond valence energy landscape (BVEL) modeling. V.K. and S.Z. conducted TEM experiments and relevant analyses. W.M.T. and T.G.H. performed AFM and s-SNOM-IR experiments and relevant analyses. D.C. performed Monte Carlo simulation. Y.W. and D.C. drafted the manuscript. All authors discussed and analyzed the results, and contributed to the manuscript.

Data Availability Statement

The data that support the findings of this study are available from the corresponding author upon reasonable request.

Keywords

cation-disordered rock salts, Li-ion batteries, metastability, over-stoichiometry

Received: July 2, 2023
Revised: October 30, 2023
Published online: October 31, 2023

[1] J. B. Goodenough, K.-S. Park, *J. Am. Chem. Soc.* **2013**, *135*, 1167.
[2] A. Manthiram, *ACS Cent. Sci.* **2017**, *3*, 1063.
[3] N. Nitta, F. Wu, J. T. Lee, G. Yushin, *Mater. Today* **2015**, *18*, 252.
[4] B. L. Ellis, K. T. Lee, L. F. Nazar, *Chem. Mater.* **2010**, *22*, 691.
[5] A. Manthiram, *Nat. Commun.* **2020**, *11*, 1550.
[6] M. S. Whittingham, *Chem. Rev.* **2004**, *104*, 4271.
[7] K. Turcheniuk, D. Bondarev, V. Singhal, G. Yushin, *Nature* **2018**, *559*, 467.
[8] C. Banza Lubaba Nkulu, L. Casas, V. Haufroid, T. De Putter, N. D. Saenen, T. Kayembe-Kitenge, P. Musa Obadia, D. Kyanika Wa Mukoma, J. M. Lunda Ilunga, T. S. Nawrot, O. Luboya Numbi, E. Smolders, B. Nemery, *Nat. Sustainability* **2018**, *1*, 495.
[9] L. Leyssens, B. Vinck, C. Van Der Straeten, F. Wuyts, L. Maes, *Toxicology* **2017**, *387*, 43.
[10] D. Chen, J. Ahn, G. Chen, *ACS Energy Lett.* **2021**, *6*, 1358.
[11] D. Chen, W. H. Kan, G. Chen, *Adv. Energy Mater.* **2019**, *9*, 1901255.
[12] J. Lee, D. A. Kitchaev, D.-H. Kwon, C.-W. Lee, J. K. Papp, Y.-S. Liu, Z. Lun, R. J. Clément, T. Shi, B. D. Mccloskey, J. Guo, M. Balasubramanian, G. Ceder, *Nature* **2018**, *556*, 185.
[13] J. Lee, A. Urban, X. Li, D. Su, G. Hautier, G. Ceder, *Science* **2014**, *343*, 519.
[14] X. Xu, L. Pi, J.-J. Marie, G. J. Rees, C. Gong, S. Pu, R. A. House, A. W. Robertson, P. G. Bruce, *J. Electrochem. Soc.* **2021**, *168*, 080521.
[15] N. Yabuuchi, M. Takeuchi, M. Nakayama, H. Shiiba, M. Ogawa, K. Nakayama, T. Ohta, D. Endo, T. Ozaki, T. Inamasu, K. Sato, S. Komaba, *Proc. Natl. Acad. Sci. USA* **2015**, *112*, 7650.
[16] K. Zhou, Y. Li, S. Zheng, M. Zhang, C. Zhang, C. Battaglia, H. Liu, K. Wang, P. Yan, J. Liu, Y. Yang, *Energy Storage Mater.* **2021**, *43*, 275.
[17] H. Li, R. Fong, M. Woo, H. Ahmed, D.-H. Seo, R. Malik, J. Lee, *Joule* **2022**, *6*, 53.
[18] R. J. Clement, Z. Lun, G. Ceder, *Energy Environ. Sci.* **2020**, *13*, 345.
[19] S. Hoshino, A. M. Glushenkov, S. Ichikawa, T. Ozaki, T. Inamasu, N. Yabuuchi, *ACS Energy Lett.* **2017**, *2*, 733.
[20] R. Chen, S. Ren, M. Knapp, D. Wang, R. Witter, M. Fichtner, H. Hahn, *Adv. Energy Mater.* **2015**, *5*, 1401814.
[21] M. A. Cambaz, B. P. Vinayan, H. Euchner, R. E. Johnsen, A. A. Guda, A. Mazilkin, Y. V. Rusalev, A. L. Trigub, A. Gross, M. Fichtner, *ACS Appl. Mater. Interfaces* **2018**, *10*, 21957.
[22] Y. Shirazi Moghadam, A. El Kharbachi, T. Diemant, G. Melinte, Y. Hu, M. Fichtner, *Chem. Mater.* **2021**, *33*, 8235.
[23] Y. Shirazi Moghadam, S. Dinda, A. El Kharbachi, G. Melinte, C. Kübel, M. Fichtner, *Chem. Mater.* **2022**, *34*, 2268.
[24] R. A. House, L. Jin, U. Maitra, K. Tsuruta, J. W. Somerville, D. P. Förstermann, F. Massel, L. Duda, M. R. Roberts, P. G. Bruce, *Energy Environ. Sci.* **2018**, *11*, 926.
[25] J. Reed, G. Ceder, *Chem. Rev.* **2004**, *104*, 4513.
[26] C. Baur, M.-E. Lacatusu, M. Fichtner, R. E. Johnsen, *ACS Appl. Mater. Interfaces* **2020**, *12*, 27010.
[27] J. H. Chang, C. Baur, J.-M. Ateba Mba, D. Arcon, G. Mali, D. Alwast, R. J. Behm, M. Fichtner, T. Vegge, J. M. Garcia Lastra, *J. Mater. Chem. A* **2020**, *8*, 16551.
[28] M. A. Cambaz, B. P. Vinayan, H. Euchner, S. A. Pervez, H. Geßwein, T. Braun, A. Gross, M. Fichtner, *ACS Appl. Mater. Interfaces* **2019**, *11*, 39848.
[29] C. Baur, I. Källquist, J. Chable, J. H. Chang, R. E. Johnsen, F. Ruiz-Zepeda, J.-M. Ateba Mba, A. J. Naylor, J. M. Garcia-Lastra, T. Vegge, F. Klein, A. R. Schür, P. Norby, K. Edström, M. Hahlin, M. Fichtner, *J. Mater. Chem. A* **2019**, *7*, 21244.
[30] V. Esposito, I. E. Castelli, *Adv. Mater. Interfaces* **2020**, *7*, 1902090.
[31] C. Gu, H.-M. Xu, S.-K. Han, M.-R. Gao, S.-H. Yu, *Chem. Soc. Rev.* **2021**, *50*, 6671.
[32] A. Sakuda, A. Hayashi, M. Tatsumisago, *Electrochemistry* **2019**, *87*, 247.
[33] F. Therrien, E. B. Jones, V. Stevanovic, *Appl. Phys. Rev.* **2021**, *8*, 031310.
[34] I. Källquist, J.-F. Martin, A. J. Naylor, C. Baur, M. Fichtner, J.-F. Colin, D. Brandell, K. Edström, M. Hahlin, *J. Phys. Chem. C* **2020**, *124*, 12956.
[35] T. Marchandier, S. Mariyappan, M. A. Kirsanova, A. M. Abakumov, G. Rousse, D. Foix, M. T. Sougrati, M. L. Doublet, J. M. Tarascon, *Adv. Energy Mater.* **2022**, *12*, 2201417.
[36] M. Freire, N. V. Kosova, C. Jordy, D. Chateigner, O. I. Lebedev, A. Maignan, V. Pralong, *Nat. Mater.* **2016**, *15*, 173.
[37] R. G. Hennig, D. R. Trinkle, J. Bouchet, S. G. Srinivasan, R. C. Albers, J. W. Wilkins, *Nat. Mater.* **2005**, *4*, 129.
[38] W. Li, L. Zheng, B. Ge, S. Lin, X. Zhang, Z. Chen, Y. Chang, Y. Pei, *Adv. Mater.* **2017**, *29*, 1605887.
[39] C. Liu, J. Cui, Z. Cheng, B. Zhang, S. Zhang, J. Ding, R. Yu, E. Ma, *Adv. Mater.* **2023**, *35*, 2209941.
[40] A. Machida, H. Saitoh, H. Sugimoto, T. Hattori, A. Sano-Furukawa, N. Endo, Y. Katayama, R. Iizuka, T. Sato, M. Matsuo, S.-I. Orimo, K. Aoki, *Nat. Commun.* **2014**, *5*, 5063.
[41] H. Wang, X. Zhang, D. Yan, C. Somsen, G. Eggeler, *Nat. Commun.* **2018**, *9*, 4017.
[42] H. Xue, C. Yang, F. De Geuser, P. Zhang, J. Zhang, B. Chen, F. Liu, Y. Peng, J. Bian, G. Liu, A. Deschamps, J. Sun, *Nat. Mater.* **2023**, *22*, 434.
[43] H. Liu, Z. Zhu, Q. Yan, S. Yu, X. He, Y. Chen, R. Zhang, L. Ma, T. Liu, M. Li, R. Lin, Y. Chen, Y. Li, X. Xing, Y. Choi, L. Gao, H. S.-Y. Cho, K. An, J. Feng, R. Kostecki, K. Amine, T. Wu, J. Lu, H. L. Xin, S. P. Ong, P. Liu, *Nature* **2020**, *585*, 63.
[44] W. Huang, L. Yang, Z. Chen, T. Liu, G. Ren, P. Shan, B.-W. Zhang, S. Chen, S. Li, J. Li, C. Lin, W. Zhao, J. Qiu, J. Fang, M. Zhang, C. Dong, F. Li, Y. Yang, C.-J. Sun, Y. Ren, Q. Huang, G. Hou, S.-X. Dou, J. Lu, K. Amine, F. Pan, *Adv. Mater.* **2022**, *34*, 2202745.
[45] D. Chen, J. Ahn, E. Self, J. Nanda, G. Chen, *J. Mater. Chem. A* **2021**, *9*, 7826.
[46] T. W. D. Farley, W. Hayes, S. Hull, M. T. Hutchings, M. Vrtis, *J. Phys.: Condens. Matter* **1991**, *3*, 4761.
[47] Y. Qiao, H. Yang, Z. Chang, H. Deng, X. Li, H. Zhou, *Nat. Energy* **2021**, *6*, 653.
[48] Y. Sun, H.-W. Lee, Z. W. Seh, N. Liu, J. Sun, Y. Li, Y. Cui, *Nat. Energy* **2016**, *1*, 15008.
[49] A. Abouimrane, Y. Cui, Z. Chen, I. Belharouak, H. B. Yahia, H. Wu, R. Assary, L. A. Curtiss, K. Amine, *Nano Energy* **2016**, *27*, 196.
[50] M. Diaz-Lopez, P. A. Chater, P. Bordet, M. Freire, C. Jordy, O. I. Lebedev, V. Pralong, *Adv. Energy Mater.* **2021**, *6*, 653.
[51] J. Du, W. Wang, A. Y. Sheng Eng, X. Liu, M. Wan, Z. W. Seh, Y. Sun, *Nano Lett.* **2020**, *20*, 546.
[52] Y. Qiao, K. Jiang, H. Deng, H. Zhou, *Nat. Catal.* **2019**, *2*, 1035.
[53] Z. Zhu, A. Kushima, Z. Yin, L. Qi, K. Amine, J. Lu, J. Li, *Nat. Energy* **2016**, *1*, 16111.
[54] Y. Wang, S. Huang, B. Raji-Adefila, A. Outka, J. H. Wang, D. Chen, *J. Am. Chem. Soc.* **2022**, *144*, 19838.
[55] A. Sifuentes, A. C. Stowe, N. Smyrl, *J. Alloys Compd.* **2013**, *580*, S271.
[56] A. K. Arora, M. Rajalakshmi, T. R. Ravindran, V. Sivasubramanian, *J. Raman Spectrosc.* **2007**, *38*, 604.
[57] G. Gouadec, P. Colomban, *Prog. Cryst. Growth Charact. Mater.* **2007**, *53*, 1.
[58] W. E. Gent, K. Lim, Y. Liang, Q. Li, T. Barnes, S.-J. Ahn, K. H. Stone, M. Mcintire, J. Hong, J. H. Song, Y. Li, A. Mehta, S. Ermon, T. Tyliszczak, D. Kilcoyne, D. Vine, J.-H. Park, S.-K. Doo, M. F. Toney, W. Yang, D. Prendergast, W. C. Chueh, *Nat. Commun.* **2017**, *8*, 2091.

[59] R. Wang, X. Chen, Z. Huang, J. Yang, F. Liu, M. Chu, T. Liu, C. Wang, W. Zhu, S. Li, S. Li, J. Zheng, J. Chen, L. He, L. Jin, F. Pan, Y. Xiao, *Nat. Commun.* **2021**, *12*, 3085.
[60] W. Weppner, R. A. Huggins, *J. Electrochem. Soc.* **2019**, *124*, 1569.
[61] A. Urban, J. Lee, G. Ceder, *Adv. Energy Mater.* **2014**, *4*, 1400478.
[62] J. Ahn, D. Chen, G. Chen, *Adv. Energy Mater.* **2020**, *10*, 2001671.
[63] S. Park, K. Jin, H. K. Lim, J. Kim, K. H. Cho, S. Choi, H. Seo, M. Y. Lee, Y. H. Lee, S. Yoon, M. Kim, H. Kim, S. H. Kim, K. T. Nam, *Nat. Commun.* **2020**, *11*, 5230.
[64] J. Zuo, C. Xu, Y. Liu, Y. Qian, *Nanostruct. Mater.* **1998**, *10*, 1331.
[65] M. Inaba, Y. Iriyama, Z. Ogumi, Y. Todzuka, A. Tasaka, *J. Raman Spectrosc.* **1997**, *28*, 613.
[66] R. A. House, G. J. Rees, K. Mccoll, J.-J. Marie, M. Garcia-Fernandez, A. Nag, K.-J. Zhou, S. Cassidy, B. J. Morgan, M. Saiful Islam, P. G. Bruce, *Nat. Energy* **2023**, *8*, 351.
[67] T. Mizokawa, Y. Wakisaka, T. Sudayama, C. Iwai, K. Miyoshi, J. Takeuchi, H. Wadati, D. G. Hawthorn, T. Z. Regier, G. A. Sawatzky, *Phys. Rev. Lett.* **2013**, *111*, 056404.
[68] F. Frati, M. O. J. Y. Hunault, F. M. F. De Groot, *Chem. Rev.* **2020**, *120*, 4056.
[69] R. Qiao, T. Chin, S. J. Harris, S. Yan, W. Yang, *Curr. Appl. Phys.* **2013**, *13*, 544.
[70] Z. Zhuo, C. D. Pemmaraju, J. Vinson, C. Jia, B. Moritz, I. Lee, S. Sallies, Q. Li, J. Wu, K. Dai, Y.-D. Chuang, Z. Hussain, F. Pan, T. P. Devereaux, W. Yang, *J. Phys. Chem. Lett.* **2018**, *9*, 6378.
[71] D. Chen, J. Wu, J. K. Papp, B. D. Mccloskey, W. Yang, G. Chen, *Small* **2020**, *16*, 2000656.
[72] Y. Kobayashi, M. Sawamura, S. Kondo, M. Harada, Y. Noda, M. Nakayama, S. Kobayakawa, W. Zhao, A. Nakao, A. Yasui, H. B. Rajendra, K. Yamanaka, T. Ohta, N. Yabuuchi, *Mater. Today* **2020**, *37*, 43.
[73] D. Chen, Unpublished, **2023**.
[74] B. Knoll, F. Keilmann, *Nature* **1999**, *399*, 134.
[75] T. Vincent, *Nat. Rev. Phys.* **2021**, *3*, 537.
[76] F. Zenhausern, Y. Martin, H. K. Wickramasinghe, **1995**, *269*, 1083.
[77] D. A. Kitchaev, Z. Lun, W. D. Richards, H. Ji, R. J. Clément, M. Balasubramanian, D.-H. Kwon, K. Dai, J. K. Papp, T. Lei, B. D. Mccloskey, W. Yang, J. Lee, G. Ceder, *Energy Environ. Sci.* **2018**, *11*, 2159.
[78] Z. Lun, B. Ouyang, Z. Cai, R. J. Clément, D.-H. Kwon, J. Huang, J. K. Papp, M. Balasubramanian, Y. Tian, B. D. Mccloskey, H. Ji, H. Kim, D. A. Kitchaev, G. Ceder, *Chem* **2020**, *6*, 153.
[79] M. A. Jones, P. J. Reeves, I. D. Seymour, M. J. Cliffe, S. E. Dutton, C. P. Grey, *Chem. Commun.* **2019**, *55*, 9027.
[80] W. H. Kan, B. Deng, Y. Xu, A. K. Shukla, T. Bo, S. Zhang, J. Liu, P. Pianetta, B.-T. Wang, Y. Liu, G. Chen, *Chem* **2018**, *4*, 2108.
[81] Z. Lun, B. Ouyang, D.-H. Kwon, Y. Ha, E. E. Foley, T.-Y. Huang, Z. Cai, H. Kim, M. Balasubramanian, Y. Sun, J. Huang, Y. Tian, H. Kim, B. D. Mccloskey, W. Yang, R. J. Clément, H. Ji, G. Ceder, *Nat. Mater.* **2021**, *20*, 214.
[82] H. Kobayashi, T. Tsukasaki, Y. Ogasawara, M. Hibino, T. Kudo, N. Mizuno, I. Honma, K. Yamaguchi, *ACS Appl. Mater. Interfaces* **2020**, *12*, 43605.
[83] H. Kobayashi, Y. Nakamura, M. Nakayama, S. Kodaki, R. Matsuo, I. Honma, *Adv. Energy Mater.* **2023**, *13*, 2203441.
[84] I. Blumenhofer, Y. Shirazi Moghadam, A. El Kharbachi, Y. Hu, K. Wang, M. Fichtner, *ACS Mater. Au* **2022**, *3*, 132.
[85] Y. Shirazi Moghadam, A. El Kharbachi, G. Melinte, T. Diemant, M. Fichtner, *J. Electrochem. Soc.* **2022**, *169*, 120514.